Acta Oceanol. Sin., 2018, Vol. 37, No. 9, P. 13–21
DOI: 10.1007/s13131-018-1261-x
http://www.hyxb.org.cn
E-mail: hyxbe@263.net

The observed tidal and residual currents in the Andaman Sea during the second half of 2016

LIU Yanliang[1, 2], GUO Jingsong[1], WANG Huiwu[1], XUE Yuhuan[1], KHOKIATTIWONG Somkiat[3], YU Weidong[2]*

[1] Center for Ocean and Climate Research, The First Institute of Oceanography, State Oceanic Administration, Qingdao 266061, China

[2] Laboratory for Regional Oceanography and Numerical Modeling, Pilot Qingdao National Laboratory for Marine Science and Technology(Qingdao), Qingdao 266237, China

[3] Phuket Marine Biological Center, Department of Marine and Coastal Resources, Phuket 83000, Thailand

Received 17 November 2017; accepted 14 March 2018

Abstract

The characteristics of currents and tidal currents in the Andaman Sea (AS) are studied during the second half of 2016 using observed data from a moored acoustic Doppler current profiler (ADCP) deployed at 8.6°N, 95.6°E. During the observation period, the mean flow is 5–10 cm/s and largely southward. The root mean square and kinetic energies of the low and high frequency flows, which are divided by a cutoff period of 5 d, are at the same level, indicating their identical importance to the total current. A power spectrum analysis shows that intraseasonal oscillations, a tidal-related semilunar month signal, a semidiurnal tidal signal and periods of 3–4 d are prominent. The barocliny of an eddy kinetic energy is stronger than the mean kinetic energy, both of which are the strongest on the bottom and the weakest at 70 m depth. Residual currents are largely southward (northward) during the summer (winter) monsoon season. Two striking peaks of the southward flow cause the 80 d period of meridional currents. The first peak is part of a large-scale circulation, which enters the AS through the northern channel and exits through the southern channel, and the second peak is part of a local vortex. The 40 d oscillation of the zonal current is forced by geostrophic variations attributed to local and equatorial remote forcing. The tidal current is dominated by semidiurnal constituents, and among these, M_2 and N_2 are the top two largest major axes. Moreover, astronomical tidal constituents MM and MSF are also significant. Diurnal constituents are weak and shallow water tides are ignorable. The aims are to introduce the new current data observed in the AS and to provide initial insights for the tidal and residual currents in the Andaman Sea.

Key words: Andaman Sea, tidal current, low frequency current

Citation: Liu Yanliang, Guo Jingsong, Wang Huiwu, Xue Yuhuan, Khokiattiwong Somkiat, Yu Weidong. 2018. The observed tidal and residual currents in the Andaman Sea during the second half of 2016. Acta Oceanologica Sinica, 37(9): 13–21, doi: 10.1007/s13131-018-1261-x

1 Introduction

Located along the eastern side of the Indian Ocean between the Malay Peninsula and the Andaman and Nicobar Islands, the Andaman Sea (AS) is characterized by a seasonal reversing monsoon, a low surface salinity and a strong internal wave frequency. The AS is part of the Asian monsoon system, which is dominated by prevailing southwest winds in summer and northeast winds in winter, and two transition periods appear in spring and autumn (De Boyer Montégut et al., 2007). The submarine topography in the AS is rather complex and makes the AS rich in internal wave excitation and complex soliton-soliton interactions (Osborne and Burch, 1980; Alpers et al., 1997).

Despite the scientific and geographical importance, the AS is one of the most poorly observed areas of the Indian Ocean. This is mainly because most areas of the AS belong to the national exclusive economic zones (EEZs) of the surrounding countries, and accessing the existing databases is prohibited by some data policy issues. Owing to the lack of observations, the AS was always of less concern than the other parts of the Indian Ocean. Yu et al. (1991) and Potemra et al. (1991) included the circulation of the AS in their numerical model studies. The former suggests that remote forcing is one of the mechanisms useful in determining the semiannual reversal of the upper ocean circulation in the eastern equatorial area of the Indian Ocean. The latter notes that the flow enters the AS through the mouth to the north of the Andaman Islands and exits through the area south of the Nicobar Islands; it is linked by a southward flow in the central AS and moves in the opposite direction from March to July. Although focused on the AS currents, these studies were mainly based on the numeric model and not validated by observations in the AS. In fact, there is almost no literature describing the observed ocean currents in the AS based on continuous long-term observations.

AS circulation is driven not only by local winds but also by the remote forcing of equatorial Kelvin waves (Yu et al., 1991; Eigen-

Foundation item: The National Key Research and Development Program of China under contract No. 2017YFC1405100; the National Natural Science Foundation of China under contract No. 41406034; the Basic Scientific Research Fund for National Public Institutes of China under contract No. GY0215P05.

*Corresponding author, E-mail: wdyu@fio.org.cn

heer and Quadfasel, 2000; Qiu et al., 2007). Using several numerical models, Chatterjee et al. (2017) note that the equatorial remote forcing attains its peak during the monsoon transition periods, when the flow enters the AS through the mouth at 6°N and exits through the mouth at 15°N (mostly) and 10°N (a small part), which is linked by a northward flow in the central AS. Their simulation of the annual cycle of currents shows that except for the monsoon transition periods, the AS circulation tends to enter the AS through the northern channel and exit through the southern channel, which is linked by a southward flow in the central AS. Altimeter data proved a way to study the surface current of the tropical oceans (Benny et al., 2015), but attributed to the uncertainty in the tidal correction, the altimeter data deteriorates on the shelf (Ray et al., 2011; Yang et al., 2016). Chatterjee et al. (2017) also note that the altimetry data cannot well describe circulations in the AS due to the vast shelf. This error is also induced to the ocean surface current analysis real-time (OSCAR) data due to its strong dependence on the altimetry data. However, they still used the OSCAR data in a qualitative sensor to validate their model results because it is the only available quasi-observed surface current data.

Large amplitude internal waves have been the focus of several studies, the basic features of which were described by *in situ* observations (Perry and Schmike, 1965; Osborne et al., 1978; Osborne and Burch, 1980) and satellite photography (Apel, 1979; Apel et al., 1985; Alpers et al., 1997). However, we are still far from completely understanding the internal waves in the AS. Although the internal waves were always caused by the strong tidal currents (Shu et al., 1986; Hyder et al., 2005), there are still no studies on the features and constituents of the tidal currents in the AS based on continuous long-term observations.

This paper introduces new current data that were observed by a set of subsurface moorings and analyzed the basic features of the upper ocean currents in the AS. The aim is to draw public attention to these observations in the AS and the efforts of the China-Thailand marine cooperation (Liu et al., 2018). The tidal and residual currents were studied using the new current data observed by the deep-water mooring. Data and methods are described in Section 2. Basic observational features are presented in Section 3. The low frequency currents are analyzed in Section 4. Tidal currents are introduced in Section 5. Finally, the summary and discussion can be found in Section 6.

2 Data and methods

The mooring used in this study was deployed on July 15 and recovered on December 26, 2016 during two China-Thailand joint cruises under the framework of the China-Thailand Joint Laboratory for Climate and Marine Ecosystem, the position of which is marked as the red triangle in Fig. 1. Most areas of Thai EEZ in the AS were covered by the broad continental shelf. The mooring was deployed on the bottom of the continental slope area, where the water depth is approximately 2 100 m. This mooring is part of a planned mooring array lies between the deep ocean and the continental shelf and includes a shallow water station near the Similan Island and a 400 m station in between.

Current data were obtained using a moored acoustic Doppler current profiler (ADCP) produced by Teledyne RD Instruments. A pitch and a roll represent the gesture of the ADCP in the water. The data can only be used when both pitch and roll are less than 15° and are of good quality if both pitch and roll are less than 5°. Figure 2 shows the pitch and roll of the ADCP installed on the mooring. Both pitch and roll were less than 3° the entire time during the study, representing the good quality of the current data.

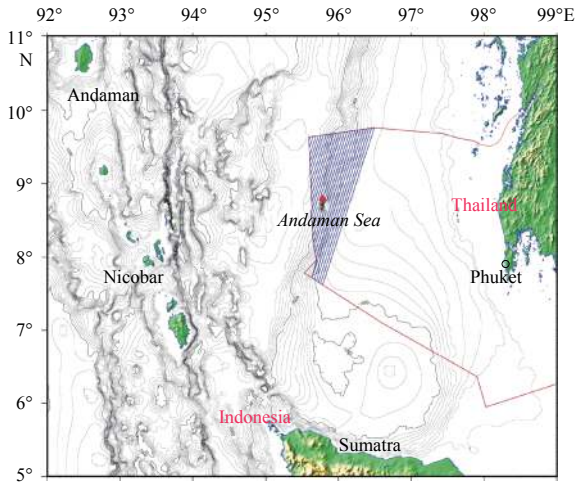

Fig. 1. Map and bathymetry of the Andaman Sea. The red line represents the exclusive economic zone (EEZ) of Thailand, and the red triangle is the position of subsurface mooring. The blue lines largely cover the cliffed continental slope in the EEZ of Thailand.

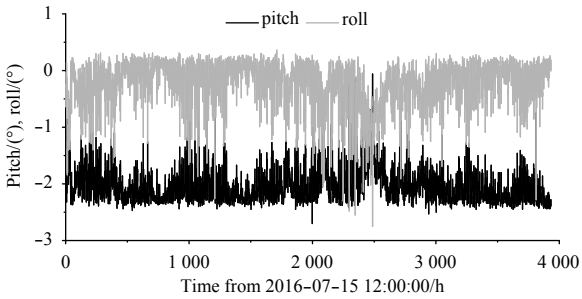

Fig. 2. Pitch and roll of the ADCP during the observation period.

The mooring was deployed at 95.6°N, 8.6°E in the central AS where the water depth was 2 100 m. The ADCP was fixed at approximately 150 m. The sampling interval was set to 1 h, and the vertical resolution was set to 4 m for the 56 bins. In fact, the actual depth had some deviation from the expected value. As shown in Fig. 3, the range of the ADCP depth was 120–260 m, and the peak probability density of the ADCP depth was approximately 145 m. According to our settings for the ADCP, there was a blind area located 8 m up from the sensor and 10 m down from the sea surface. Therefore, we analyzed the current data from 130 to 20 m at 10 m interval using a vertical linear interpolation.

The routine package provided by Foreman (1978) was used to calculate the tidal ellipses and phase lags of the tidal constituents, coupling the least squares procedure with adjustment of the number of tidal constituents. The maximum number of tidal constituents is 146; among these, 101 are shallow water tidal constituents. A 120 h low-pass filter was used to gain the residual current.

To examine the barocliny of the residual current, the ratio (R_{mke}) of the mean depth-dependent kinetic energy to the total mean kinetic energy and the ratio (R_{eke}) of the mean depth-dependent eddy kinetic energy to the total eddy kinetic energy is calculated following the method of Teague et al. (1998):

$$R_{\mathrm{mke}}(z) = \frac{\bar{u}_{\mathrm{dd}}^2(z) + \bar{v}_{\mathrm{dd}}^2(z)}{\bar{u}^2(z) + \bar{v}^2(z)}, \tag{1}$$

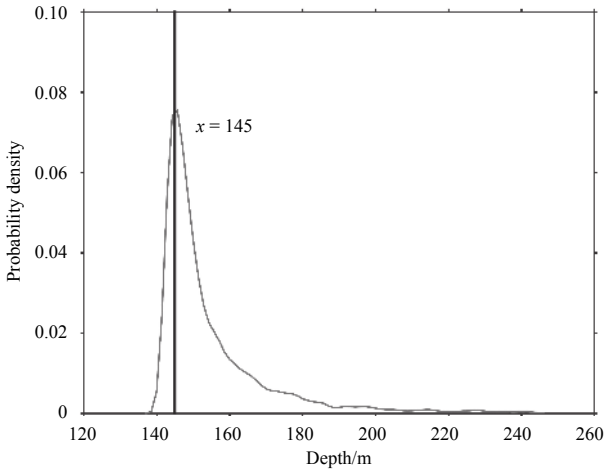

Fig. 3. Probability density of the depth of ADCP.

$$R_{\mathrm{eke}}(z)=\frac{\overline{u_{\mathrm{dd}}^{'2}}(z)+\overline{v_{\mathrm{dd}}^{'2}}(z)}{\overline{u^{'2}}(z)+\overline{v^{'2}}(z)}. \tag{2}$$

The observed zonal and meridional current speeds u and v, functions of depth z and time t, are constituents of their barotropic (u_{bt}) and depth-dependent (u_{dd}) parts:

$$u(z,t)=u_{\mathrm{bt}}(t)+u_{\mathrm{dd}}(z,t), \tag{3}$$

among them, the zonal depth-dependent current speed u_{dd} can also be decomposed into two parts:

$$u_{\mathrm{dd}}(z,t)=\bar{u}_{\mathrm{dd}}(z)+u_{\mathrm{dd}}{}'(z,t), \tag{4}$$

where the time-mean of the depth-dependent part of velocity can be calculated as follows:

$$\bar{u}_{\mathrm{dd}}(z)=\frac{1}{T}\int_0^T u_{\mathrm{dd}}(z,t)\,\mathrm{d}t. \tag{5}$$

The variance of the depth-dependent part of velocity is

$$\overline{u_{\mathrm{dd}}^{'2}}(z)=\frac{1}{T}\int_0^T u_{\mathrm{dd}}^{'2}(z,t)\,\mathrm{d}t, \tag{6}$$

and the total variance is

$$\overline{u^{'2}}(z)=\frac{1}{T}\int_0^T u^{'2}(z,t)\,\mathrm{d}t. \tag{7}$$

3 Basic characteristics of current

The AS is part of the Asian monsoon system and is controlled by the seasonal reversing monsoon. Figure 4 shows the zonal and meridional wind speeds at the observation location. From January to early March, northeast winds prevailed in the AS. A transition period appeared from March to May, which was characterized by a weak wind. The summer monsoon lasted from late May to late October when the strong southwest winds prevailed in the AS. The autumn transition period was very short during early November and was followed by the northeast winter monsoon beginning in mid-November. During the summer monsoon season, the zonal components were strikingly stronger than the meridional part.

The AS is among the areas of maximum summer precipitation in the Indian Ocean (Qi and Wang, 2015); plenty of rainfall and large river inflow from the Irrawaddy River bring large amounts of fresh water and yield a rather low surface salinity. The surface salinity was observed to be 32 on December 26, 2016 (Fig. 5), and there was a strong halocline from 30 to 70 m, making the mixed layer very shallow (≈30 m) and forming a barrier layer below. The thermocline was located between 75 and 140 m.

The time-averaged currents were largely southward (Fig. 6). From 20 to 130 m, the change in the current direction was minimal. There was a westerly above the thermocline and a slight easterly below it. The current speed was the largest on the surface (9–10 cm/s at 20 m). It decreased with the increase in seawater depth above the thermocline but ceased dropping at 80 m. As mentioned above, the southwest monsoon stopped at the end of October, and most of the observation period were within the summer monsoon season. In the open ocean of the Northern Hemisphere, west winds tend to drive a southward current, while east winds tend to form a northward current. The wind-driven southward current during the summer monsoon season made the mean flow southward and stronger on the surface.

The detailed statistical information of the currents is listed in

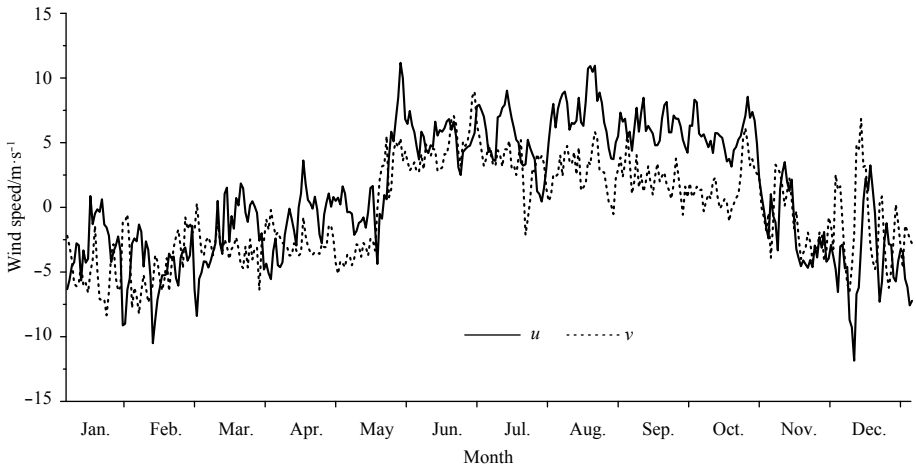

Fig. 4. Zonal (solid line) and meridional (dotted line) wind speeds at the observation location.

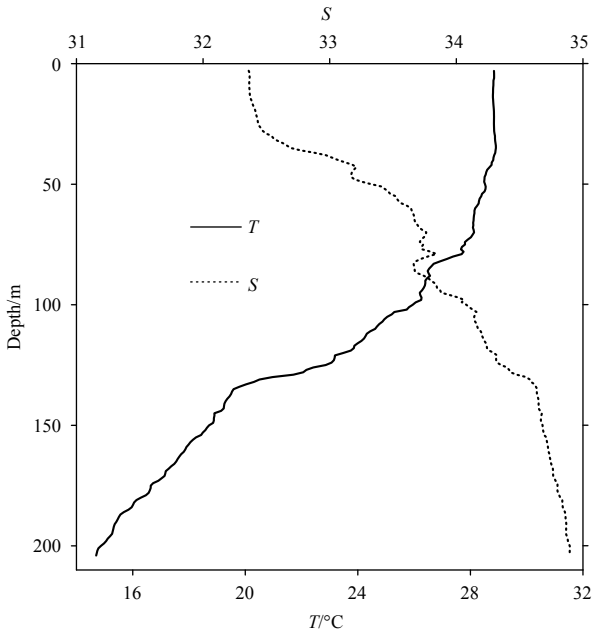

Fig. 5. Temperature (T)-salinity (S) profile observed at the mooring site on December 26, 2016. The solid and dashed lines represent the temperature and salinity profiles, respectively.

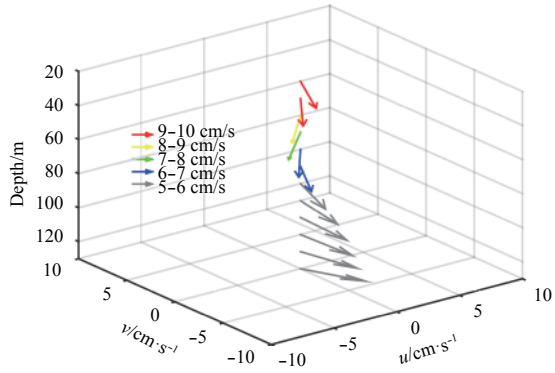

Fig. 6. Mean current at 10 m intervals of depth from 20 to 130 m during the observation period. Different colors represent the levels of the current velocity.

Table 1. The observed current speed contains not only the signals of the tidal and residual currents but also the signals of the instantaneous wind and currents caused by internal waves. The maximum current speeds at all levels were in the range of 50–90 cm/s; among these, the largest speed is 89.4 cm/s at the depth of 20 m. The mean meridional component $\bar{u}$ was always negative, the value of which was prominently larger ($\geqslant$8 cm/s) in the mixed layer and relatively small and homogeneous below it. The mean zonal part $\bar{u}$ was weaker than $\bar{v}$ at all depths, except for 50 m. In the thermocline, $\bar{u}$ was very weak, especially at depths of 100 and 110 m; the value was only 0.3 m/s, and as a result, the mean current was dominated by the southward flow. With a cutoff period of 5 d, the mean values of the root mean square (RMS) of low frequency flow (12.3 cm/s) and high frequency flow (11.2 cm/s) were at the same level, as well as the mean kinetic energy (162 and 124 cm^2/s^2, respectively), indicating their identical contributions to the total current. The mean low-pass filtered currents were similar to the mean raw current. The RMS of the meridional current (σ_v) had a similar vertical pattern with $\bar{v}$, and it was larger than σ_u at all levels. Although σ_u was also relatively small in the thermocline, the value was only reduced by a small percentage. The RMS of low frequency meridional current (σ_{v_l}) was higher than σ_{u_l}, but the RMS of high frequency meridional current (σ_{v_h}) was similar to σ_{u_h}. The $\sigma_{u_l}$was larger in the top 60 m and smaller below this level than σ_{u_h}, while σ_{v_l} was larger than σ_{v_h} at all levels. The mean kinetic energy of the low frequency current decreased from the surface to the bottom, while that of the high frequency current was nearly homogeneous at all levels.

A rotary spectral analysis was performed to detect the dominant frequencies of the observed currents (Fig. 7). Both zonal and meridional components of the currents had three common periods, i.e., 14.5 d, 12 h and 3 d. The 14.5 d can be the semi-lunar month variation of spring-neap tides, the 12 h period can be considered the signal of semiannual tides and the 3 d signal appeared only in the thermocline below 80 m and can be associated with the astronomical tides. The most prominent signal was the intraseasonal oscillation, which was centralized at Day 40 in the zonal current and Day 80 in meridional current. The 40 d period in zonal current was strong in the upper 100 m, while the 80 d period in meridional current was strong at all depths.

To quantify the degree of depth dependence of the observed

Table 1. Statistics of current velocities

Depth/m	$(\bar{u}/\sigma_u)$/cm·s^{-1}	$(\bar{v}/\sigma_v)$/cm·s^{-1}	$(\overline{u_l}/\sigma_{u_l})$/cm·s^{-1}	$(\overline{v_l}/\sigma_{v_l})$/cm·s^{-1}	$(\overline{u_h}/\sigma_{u_h})$/cm·s^{-1}	$(\overline{v_h}/\sigma_{v_h})$/cm·s^{-1}	S_{max}/cm·s^{-1}	E_l/cm^2·s^{-2}	E_h/cm^2·s^{-2}
20	−4.4/17.0	−8.9/22.9	−4.4/12.2	−8.8/19.6	0.0/11.6	−0.0/11.6	89.4	266	134
30	−5.7/16.8	−8.0/21.8	−5.8/12.2	−8.1/18.5	0.0/11.3	−0.0/11.3	74.2	245	128
40	−6.1/16.5	−6.5/20.7	−6.1/12.4	−6.5/17.2	−0.0/10.7	−0.0/11.4	82.0	224	121
50	−5.6/16.2	−5.4/19.6	−5.6/12.4	−5.5/16.0	−0.0/10.4	−0.0/11.1	67.1	204	116
60	−4.4/15.2	−5.4/18.7	−4.4/11.3	−5.5/15.0	−0.0/10.1	0.0/11.1	80.2	175	112
70	−3.1/14.8	−5.5/18.5	−3.1/10.3	−5.6/14.7	0.0/10.6	0.0/11.2	68.7	161	118
80	−1.9/14.3	−5.4/18.6	−1.9/9.3	−5.5/14.1	0.0/10.8	0.0/11.9	75.0	143	129
90	−0.9/14.3	−5.7/18.1	−1.0/8.9	−5.7/13.7	0.0/11.2	−0.0/11.7	73.9	133	130
100	−0.3/13.5	−5.9/17.9	−0.2/8.0	−6.0/13.4	−0.0/10.8	−0.0/11.8	68.8	121	127
110	0.3/12.9	−5.9/17.3	0.2/6.7	-5.9/12.7	0.1/11.0	−0.0/11.6	85.0	103	127
120	1.1/12.9	−5.3/16.7	1.1/5.9	−5.3/12.2	0.1/11.5	−0.0/11.3	61.4	91	130
130	2.2/12.5	−5.0/16.3	2.2/5.8	−5.0/12.1	0.1/11.1	−0.0/10.9	50.4	89	120

Note: $\bar{u}/\sigma_u$, $\bar{v}/\sigma_v$, $\overline{u_l}/\sigma_{u_l}$, $\overline{v_l}/\sigma_{v_l}$, $\overline{u_h}/\sigma_{u_h}$ and $\overline{v_h}/\sigma_{v_h}$represent the mean zonal and meridional components and their root mean square values (RMS) of the raw current velocities, the 5 d low-pass filtered current velocities, and the 5 d high-pass filtered current velocities. The S_{max}, E_l and E_h are the maximum current speed, kinetic energy of low frequency current and high frequency current, respectively.

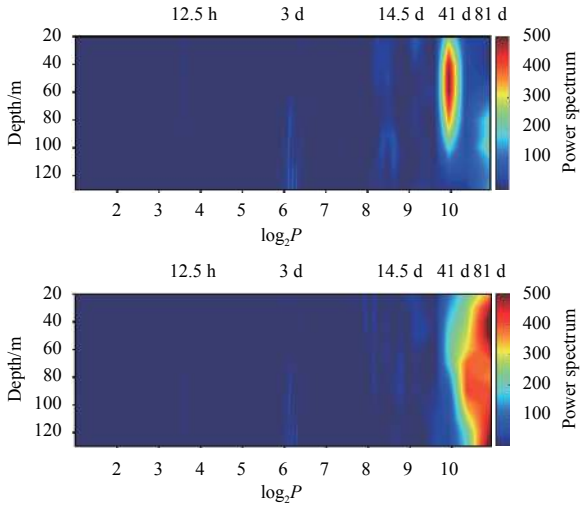

Fig. 7. Power spectrum of zonal (upper) and meridional (lower) components of current velocity. The x-axis is the logarithm of periods (P) (in hours) to Base 2.

currents, the method of Teague et al. (1998) was used to calculate the ratio (R_{mke}) of the mean depth-dependent kinetic energy to the total mean kinetic energy and the ratio (R_{eke}) of the mean depth-dependent eddy kinetic energy to the total eddy kinetic energy. The mean R_{mke} was 0.15, about half as large as the mean R_{eke}, which was nearly 0.3 (Fig. 8). In fact, the depth dependence of the mean kinetic energy was weaker than that of the eddy kinetic energy throughout the water column. The trend of R_{mke} and R_{eke} were similar with each other, both of which were strongest on the bottom of the water column and weakest at approximately 70 m near the top of thermocline (TTD), which was a significant turning point. Whether the movement was upward or downward from the TTD, the depth dependence became stronger. Furthermore, the R_{mke} showed another turning point at 50 m, from which the depth dependence became weaker to the top.

4 Non-tidal currents

For analyzing the low frequency current flow, a 5 d low-pass filter was used to remove the high frequency flow from the raw observations. This is different from some other studies (Teague et al., 1998; Wang et al., 2011) where a cutoff frequency of 40 h was used. This is because the mechanism of the 3–4 d fluctuation in the thermocline was still not clear, which should be discussed more in the future. During the summer monsoon season, a southward flow is dominant most of the time (Fig. 9), which is consistent with the results of Chatterjee et al. (2017), who show that two weak northwestward flows appear during late August and early October. However, the northward flow dominated the winter monsoon season, which is different from Chatterjee et al. (2017) but consistent with the OSCAR data (Fig. 10a). The most striking phenomenon was the two peaks of the southward currents that occurred during middle July to middle August and middle October to middle November, respectively. These two peaks were the main cause of the 81 d spectrum peak of the meridional component of the currents. The former was weakened with depth, while the latter was strongest in the range of thermocline. The phase of the former was uniform from the surface to the bottom, but a phase lag of approximately 10 d between depths of 20 and 130 m existed in the latter. The zonal component of the currents had several westward peaks that occurred in middle August, late September and late November, respectively, which were accompanied by weak northward flow components and a prominent decreasing trend from top to bottom. The largest northward flow appeared in early December.

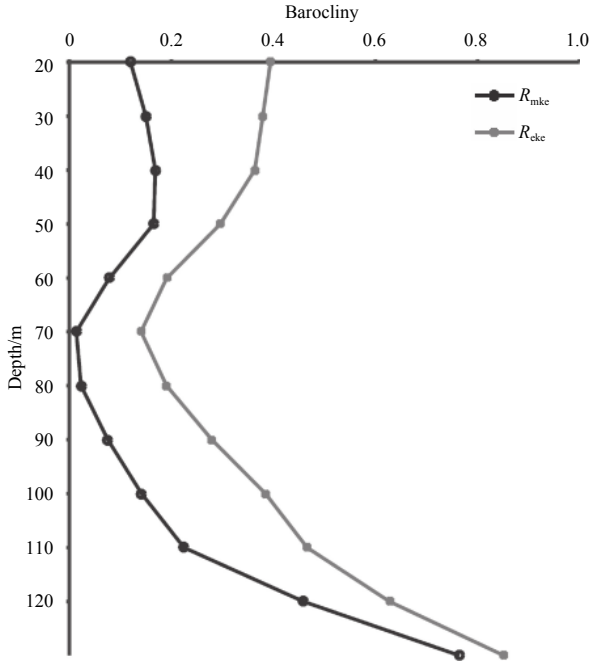

Fig. 8. The barocliny of the mean kinetic energy represented by the ratio of the mean baroclinic kinetic energy to the mean kinetic energy and the barocliny of the eddy kinetic energy described by the ratio of the mean baroclinic eddy kinetic energy to the mean eddy kinetic energy.

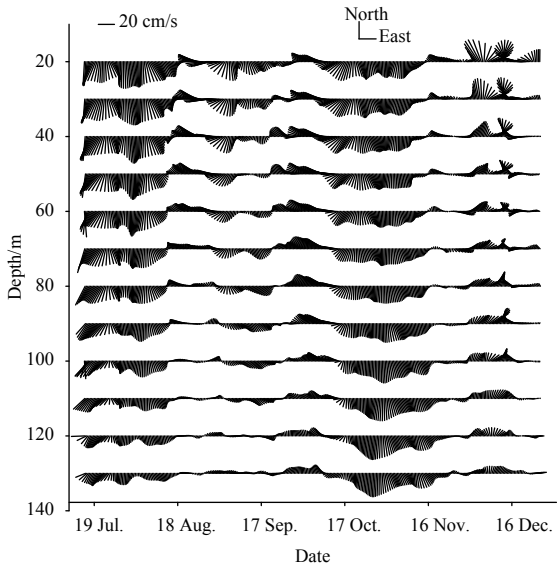

Fig. 9. Vector-stick diagram of low frequency current velocities at different depths, which were calculated by a 5 d low-pass filter.

Despite the uncertainty, the OSCAR data were included to qualitatively explain the two striking peaks in the southward flow. The trend of the OSCAR data was largely consistent with the mooring-observed current with a correlation coefficient (r) of

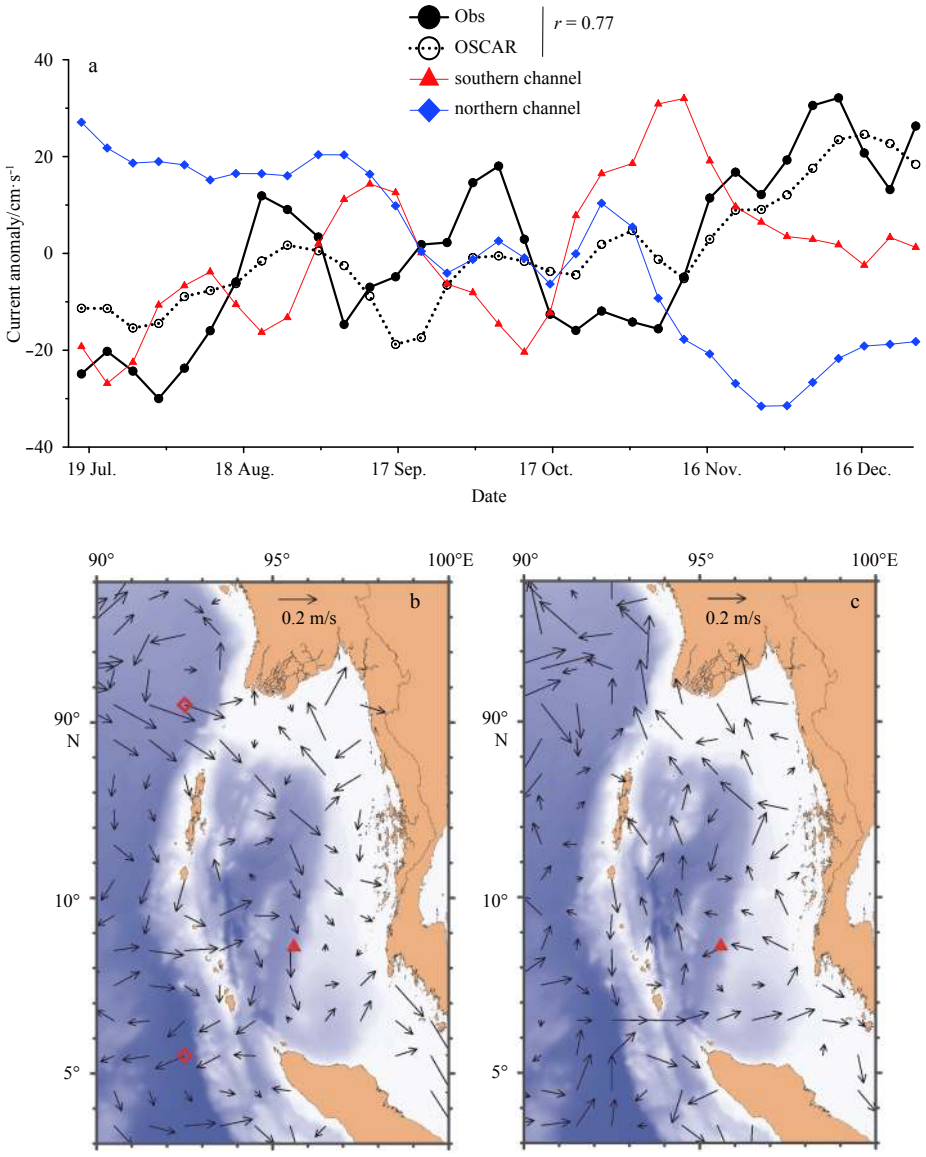

Fig. 10. Time series and vectorgraphs of currents in the AS. a. Comparison of pentad surface current speed in the central AS and northern and southern mouths between the AS and Bay of Bengal. The black solid line represents the meridional component of currents observed by the mooring; the black dotted line represents the meridional component of currents from the OSCAR at the same position as the mooring; and the red and blue lines represent the zonal current at the southern and northern mouths. The positive values represent the eastward and northward flows of meridional and zonal currents. b. The vector diagram of mean surface current during the first southward peak in the current (July 16 to August 15). c. The vector diagram of mean surface current during the second southward peak in the current (October 17 to November 11).

0.77. However, due to the uncertainty of the altimetry data, the difference between them was also notable (Fig. 10a). The first peak of the southward flow from July 16 to August 15 (P1) was coincident with the peak westward flow at the southern mouth and the eastward flow at the northern mouth. Figure 10b also shows the flow entering the AS from the northern mouth and exiting through the southern mouth, which is linked to a strong southward flow in the central AS. Different from the P1 that was caused by the large-scale circulation in the northeastern Indian Ocean, the second peak from October 17 to November 11 (P2) seemed to be part of a local vortex in the AS. During P2, the eastward flow through the southern channel reached its peak. Although the zonal flow through the northern channel was slightly eastward, the flow exited through the northern channel in the form of a strong northward current (shown in Fig. 10c). However, there was a counterclockwise local vortex between 6° and 10°N, and the mooring was just deployed to the west side. The second peak of the southward flow was caused by this local vortex. It is worth mentioning that the southward current of the OSCAR data was much weaker than the mooring-observed current during P2, which reflects the uncertainty of the altimetry-based OSCAR data.

To clarify the dominant factors of the zonal current variation, the correlation coefficients with the local and central Indian Ocean (CIO) sea level anomaly (SLA), as well as the wind speeds are listed in Table 2. The zonal current was significantly correlated with the local SLA gradient and meridional wind speeds, as well as the SLA (lagged for 23 d) in the central Indian Ocean, in-

Table 2. Correlation test between the zonal daily current and the SLA, as well as the wind speed in the AS and the central Indian Ocean (CIO)

	SLA			Wind			
	Local	CIO	Gradient	U_{local}	V_{local}	U_{CIO}	V_{CIO}
R	0.326	0.276	0.437	0.097	0.445	0.045	0.031
P	1.8×10^{-5}	8.3×10^{-4}	4.3×10^{-9}	0.217	2.3×10^{-9}	0.404	0.596

Note: The gradient is the meridional gradient of SLA at the mooring location in the AS. The domain of the CIO was 2.5°S–2.5°N, 80°–90°E. There was a 23 d lag in all the equatorial parameters.

dicating the importance of both local and remote forcing. However, its correlation coefficients with both meridional local winds and SLA gradient were much larger than that with SLA in the central Indian Ocean. Thus, the zonal currents were considered to be influenced primarily by local processes, and secondarily by the remote forcing from the equatorial Indian Ocean.

The power spectrum density and 95% confidence interval of the meridional gradient of the SLA and the meridional wind speed at the mooring location are shown in Fig. 11. The meridional wind speed was dominated by 80 d variations, while the 40 d period was within the 95% confidence level. The SLA was dominated by the 40 d variations, coinciding with the zonal current observed by the mooring, while the 80 d and 12 d signals were also significant. Thus, the 40 d oscillation of the zonal current was considered to be caused by geostrophic variations. Forced by local winds and equatorial remote forcing (Yu, 2003; Cheng et al., 2013), The long-term variation of the SLA in the AS is worth future study.

5 Tidal currents

The tidal routine package of Foreman uses a least squares analysis method incorporating nodal modulation, inference calculation and astronomical argument correction to evaluate the tidal ellipses. The maximum number of possible tidal constituents that can be included in the tidal analysis is 146.

Table 3 shows the major axes of the top ten tidal constituents; among these, the semidiurnal constituents M_2 (7–9 cm/s) and S_2 (3–4 cm/s) are the largest, followed by the astronomical tidal constituents MM (1–3 cm/s) and MSF (1–3 cm/s). The diurnal tidal constituent K_1 (1–2 cm/s) and semidiurnal constituents N_2 (1–2 cm/s) and ETA_2 (1–2 cm/s) were in the third echelon. As the strongest constituent, M_2 had the largest major axes that were more than twice as large as N_2, which was the second largest. The major axes of most constituents decreased from the surface to the bottom, except for ETA_2 and UPS_1. The shallow water constituents were weak at the deep-water station.

The tidal ellipses of the top seven constituents were plotted (Fig. 12) according to the major and minor semi-axes, inclination angles (semi-major axis rotation measured in degrees counterclockwise from the east) calculated by the routine package. The two largest semidiurnal constituents, M_2 and S_2, rotated clockwise throughout the water column. The ellipses of M_2 were

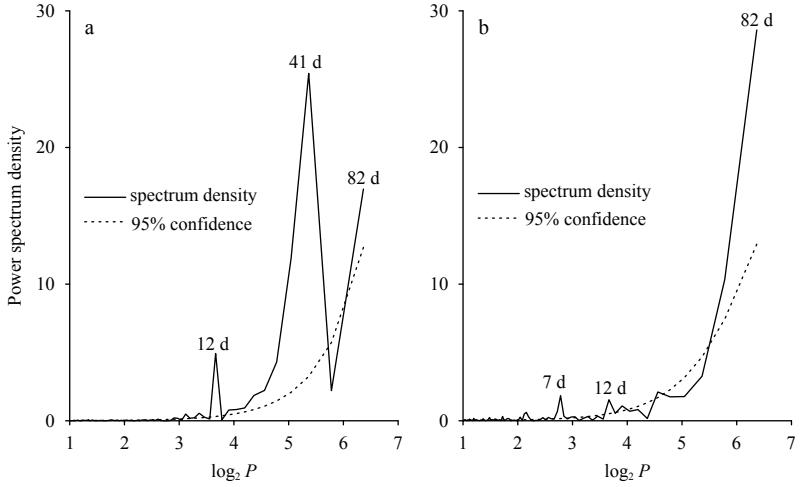

Fig. 11. Power spectrum density and 95% confidence interval of meridional gradient of SLA (a) and meridional wind speed at the mooring location (b). The *x*-axis is the logarithm of periods (in day) to Base 2.

Table 3. Major axes of Top 10 tidal ellipses

Depth/m	Name of Top 10 tide constituents									
	M_2	S_2	MM	MSF	K_1	N_2	ETA_2	L_2	O_1	UPS_1
20	9.148	4.472	3.281	2.609	1.676	2.232	1.669	1.599	0.717	1.163
40	9.601	4.470	3.634	2.828	2.000	2.193	1.380	1.461	1.077	0.857
60	9.231	3.892	2.318	3.131	1.773	2.061	1.493	1.029	0.771	0.512
80	8.735	3.916	1.428	2.761	1.612	1.902	1.706	0.853	1.063	0.992
100	7.091	3.597	1.948	1.655	1.196	1.949	1.087	0.641	0.202	1.312
120	6.627	2.853	1.605	1.119	0.917	1.642	1.337	0.758	0.556	1.027

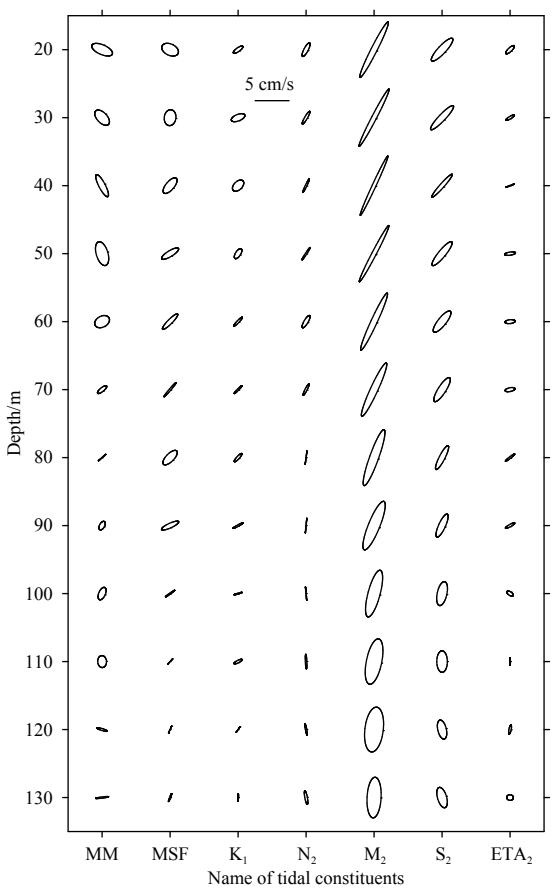

Fig. 12. Tidal current ellipses of the seven main tidal constituents at depth intervals of every 10 m from 20 to 130 m. The solid ellipses represent the clockwise rotation of the current vectors of tidal constituents, while the dashed ellipses represent the counterclockwise rotation.

oblate above the thermocline, indicating a strong, reciprocating current. Although the major axes were short in the thermocline, the minor axes were longer, and as a result, the total kinetic energy showed minimal change. The dip angles of the major axes of both M_2 and S_2 had a counterclockwise rotation from the surface to the bottom. The rotating direction of the tidal currents of two astronomical tidal constituents were opposite of each other. The MM currents rotated counterclockwise in the thermocline and clockwise above it, while the MSF currents rotated clockwise in the thermocline and counterclockwise above it. Current ellipses for K_1, N_2 and ETA_2 were generally small and counterclockwise.

6 Summary

The Andaman Sea (AS) is characterized by a monsoonal climate, plenty of fresh water and strong internal waves. Although important for science and geography, it is a rather poor observation area. The aim of this paper was to introduce new current data and provide the first insights into AS currents. On the basis of the observed data from a moored ADCP deployed during the second half of 2016 at 8.6°N, 95.6°E, the basic characteristics of currents in the AS, specifically tidal and residual currents, were studied. The thermocline, which was found to be an important turning point in the current profiles, was in a range of 70–130 m, which was inferred from the temperature-salinity profile through CTD observation.

During the observation period, the largest current speed was 89 cm/s. The mean flow, which was 5–6 cm/s in the range of the thermocline and 9–10 cm/s at depths of 20–30 m, was largely southward throughout the water column. The RMS and kinetic energies of both low frequency flow and high frequency flow were divided by a cutoff period of 5 d and were at the same level, indicating their identical importance to the absolute current. Intraseasonal oscillation was found to be the most significant signal in the power spectrum of both the zonal current speed and meridional current speed, the main periods of which were 40 d and 80 d, respectively. Furthermore, the semidiurnal period of 12.5 h was also significant throughout the water column, while a 3–4 d period was found to be prominent in the range of the thermocline. The barocliny of the eddy kinetic energy was stronger than the mean kinetic energy, both of which were strongest on the bottom and weakest at the top of thermocline. The low frequency flows were largely southward during the summer monsoon season and northward during the winter monsoon season, which is consistent with the OSCAR data. The two peaks of the meridional current speed during the middle of July to the middle of August and the middle of October to early November were focused, the former of which was caused by large-scale circulation that entered the AS through the northern channel, connecting the AS and the BOB and exiting through the southern channel. The latter was part of a local vortex at 7°–10°N. The 40 d oscillation of the zonal current was caused mainly by geostrophic variations attributed to local and equatorial remote forcing. The tidal current was dominated by the semidiurnal constituents, and among these, M_2 and N_2 were the top two largest major axes. The astronomical tidal constituents MM and MSF were also significant. The diurnal constituents were weak.

Some scientific issues need to be studied further in the future. First, the 3–4 d period in the thermocline may be partly due to the astronomical tidal constituents, but the main cause needs to be elucidated. Second, the variations in the local vortex need to be studied further. Thirdly, the seasonal variation of the remote forcing needs to be further clarified.

Acknowledgements

This study is under the framework of the international cooperation projects monsoon onset monitoring and its social and ecosystem impact (MOMSEI) and ocean forecasting and marine disasters mitigation system for Southeast Asia seas (OFS). The organizers and participants of the joint cruise from the Phuket Marine Biological Center and the First Institute of Oceanography, State Oceanic Administration are much appreciated for their excellent support. The wind and sea level anomaly data referred in this paper were from NCEP/NCAR reanalysis (https://www.esrl.noaa.gov/psd/data/reanalysis/) and AVISO (https://www.aviso.altimetry.fr/), respectively.

References

Alpers W, Heng Wangchen, Hock L. 1997. Observation of internal waves in the Andaman Sea by ERS SAR. In: Proceedings of Remote Sensing- A Scientific Vision for Sustainable Development, 1997 IEEE International Geoscience and Remote Sensing. Singapore: IEEE, 1518–1520

Apel J R. 1979. Observations of internal waves surface signatures in ASTP photographs. Apollo- Soyuz Test Project Summary Science Report Volume II, NASA SP 412

Apel J R, Thompson D R, Tilley D G, et al. 1985. Hydrodynamics and radar signatures of internal solitons in the Andaman Sea. John Hopkins APL Technical Digest, 6(4): 330–337

Benny N P, Shenbakavalli R, Mazlan H, et al. 2015. Mesoscale surface

circulation and variability of southern Indian Ocean derived by combining satellite altimetry and drifter observations. Acta Oceanologica Sinica, 34(9): 12–22

Chatterjee A, Shankar D, McCreary J P, et al. 2017. Dynamics of Andaman Sea circulation and its role in connecting the equatorial Indian Ocean to the Bay of Bengal. Journal of Geophysical Research, 122(4): 3200–3218, doi: 10.1002/2016JC012300

Cheng Xuhua, Xie Shangping, McCreary J P, et al. 2013. Intraseasonal variability of sea surface height in the Bay of Bengal. Journal of Geophysical Research, 118(2): 816–830

De Boyer Montégut C, Mignot J, Lazar A. 2007. Control of salinity on the mixed layer depth in the world ocean: 1. General description. Journal of Geophysical Research, 112(C6): C06011, doi: 10.1029/2006JC003953

Eigenheer A, Quadfasel D. 2000. Seasonal variability of the Bay of Bengal circulation inferred from Topex/Poseidon altimetry. Journal of Geophysical Research, 105(C2): 3243–3252

Foreman M G G. 1978. Manual for tidal currents analysis and prediction. Sydney: Institude of Ocean Sciences

Hyder P, Jeans D R G, Cauquil E, et al. 2005. Observations and predictability of internal solitons in the northern Andaman sea. Applied Ocean Research, 27(1): 1–11

Liu Yanliang, Li Kuiping, Ning Chunlin, et al. 2018. Observed seasonal variations of the upper ocean structure and air-sea interactions in the Andaman Sea. Journal of Geophysical Research, 123(2): 922–938

Osborne A R, Burch T L. 1980. Internal solitons in the Andaman Sea. Science, 208(4443): 451–460

Osborne A R, Burch T L, Scarlet R I. 1978. The influence of internal waves on deep-water drilling. Journal of Petroleum Technology, 30(10): 1497–1504

Perry R B, Schmike G R. 1965. Large-amplitude internal waves observed off the northwest coast of Sumatra. Journal of Geophysical Research, 70(10): 2319–2324

Potemra J T, Luther M E, O'Brien J J. 1991. The seasonal circulation of the upper ocean in the Bay of Bengal. Journal of Geophysical Research, 96(C7): 12667–12683

Qi Li, Wang Yuqing. 2015. Discrepancies in different precipitation data products in the Bay of Bengal during summer monsoon season. Advances in Meteorology, 2015: 806845

Qiu Yun, Li Li, Yu Weidong, et al. 2007. Annual and interannual variations of sea-level anomaly in the Bay of Bengal and the Andaman Sea. Acta Oceanologica Sinica, 26(6): 13–29

Ray R D, Egbert G D, Erofeeva S Y. 2011. Tide predictions in shelf and coastal waters: status and prospect. In: Vignudelli S, Kostianoy A G, Cipollini P, et al., eds. Coastal Altimetry. Berlin: Springer, 191–216, doi: 10.1007/978-3-642-12796-0_8

Shu Xingbei, Geng Shijiang, Gu Xuejun, et al. 1986. Verification of internal waves in offshore areas by means of current observations. Acta Oceanologica Sinica, 5(2): 165–172

Teague W J, Perkings H T, Hallock Z R, et al. 1998. Current and tide observations in the southern Yellow Sea. Journal of Geophysical Research, 103(C12): 27783–27793

Wang Huiwu, Chen Hongxia, Lv Liangang, et al. 2011. Study of tide and residual current observations in Chukchi Sea in the summer 2008. Haiyang Xuebao (in Chinese), 33(6): 1–8

Yang Guang, He Hailun, Wang Yuan, et al. 2016. Evaluating a satellite-based sea surface temperature by shipboard survey in the northwest Indian Ocean. Acta Oceanologica Sinica, 35(11): 52–58

Yu Lisan. 2003. Variability of the depth of the 20 °C isotherm along 6 °N in the Bay of Bengal: its response to remote and local forcing and its relation to satellite SSH variability. Deep-Sea Research II: Topical Studies in Oceanography, 50(12–13): 2285–2304

Yu Lisan, O'Brien J J, Yang Jiayan. 1991. On the remote forcing of the circulation in the Bay of Bengal. Journal of Geophysical Research, 96(C11): 20449–20454